Progress In Electromagnetics Research, Vol. 122, 341–360, 2012

A 3D TARGET IMAGING ALGORITHM BASED ON TWO-PASS CIRCULAR SAR OBSERVATIONS

L. J. Yu[1], [2], [*] and Y. H. Zhang[2]

[1]Graduate University of the Chinese Academy of Sciences, Beijing 100039, China

[2]The Key Laboratory of Microwave Remote Sensing, Chinese Academy of Sciences, Beijing 100190, China

Abstract—In circular synthetic aperture radar (CSAR), the radar collects data over a circular not a linear trajectory. The two-dimensional (2D) CSAR image also contains three-dimensional (3D) information about the target. In this paper, we propose an imaging algorithm for 3D target reconstruction with two-pass CSAR observations so as to overcome the problem of limited azimuthal persistence for real anisotropic targets, and avoid the assumption that target falls into the same resolution cell for each elevation pass when multi-pass observations are used. In the algorithm, the first step is to divide both of the two full-aperture CSAR data into subapertures in the same way; the second step is to obtain, for each subaperture, the height of target according to the established relationship between the pixel displacements in the image pair of two observations on the same focal plane and the pixel displacements in the image pair of one observation on two different focal planes; the third step is to obtain the 3D target coordinates based on the retrieved height information and the 2D image coordinates; the last step is to get the final 3D image by combining the obtained 3D images of all subapertures. The results of point target simulation indicate that the 3D information (both amplitudes and positions) are well reconstructed. At the same time, the processing results of backhoe data simulated by the Xpatch software show that the outline of the 3D structure is also well reconstructed although the available data corresponding to the depressing angles are not as good as expected.

Received 19 October 2011, Accepted 14 November 2011, Scheduled 24 November 2011

[*] Corresponding author: Lingjuan Yu (yljsmile@163.com).

1. INTRODUCTION

In circular synthetic aperture radar (CSAR), the radar illuminates targets over a complete 360 degree aperture. This wide-angle non-linear collection geometry makes CSAR can obtain both two-dimensional (2D) high resolution image and three-dimensional (3D) image [1–3]. Due to these unique features, CSAR has been widely used in some special situations, such as, automatic target recognition (ATR) system for tank or vehicles [1], high resolution imaging of building or urban area [4], detection of targets in the foliage or under the ground [5], detection of concealed objects in airport security systems [6, 7], and geosynchronous Circular SAR (GeoCSAR) imaging [8].

Because of the curved aperture, classical algorithms, e.g., range Doppler (RD) algorithm [9], chirp scaling (CS) algorithm [10], and range migration algorithm (RMA) [11, 12], cannot be directly applied to CSAR imaging. An algorithm based on the Fourier properties of slant plane Green function was presented by Soumekh for CSAR [1, 13]. But it involves the unstable pseudo-inversion of the system kernel matrix. Although a confocal algorithm presented by Ishimaru et al. can be applied for arbitrary geometry [2], it is impractical due to computational inefficiency. The back projection (BP) algorithm can also be adapted to arbitrary geometry and has been widely used in CSAR imaging [3, 14, 15]. In order to extract the height information from single pass CSAR data, one method based on the pixel displacements between different sub-aperture 2D images was presented by Oriot and Hubert [16]. But it is inefficient and a limited 3D resolution can be achieved for real anisotropic targets.

One way to improve 3D resolution is to add another aperture in height direction, which is known as elevation and circular synthetic aperture radar (E-CSAR) system proposed by Soumekh [1]. The corresponding imaging algorithm based on Fourier decomposition was also presented. But it is hard for airborne CSAR to satisfy the acquisition condition of this system, and the processing of large scale data is very time-consuming. Another interferometric way to improve 3D resolution was considered by Ertin et al. [17, 18]. However, the real flight paths are non-uniform elevation spacing and non-constant elevation throughout the circular passes. A sparsity regularized interpolation is then presented to solve these problems by Ertin et al. and his research group [19–21].

Among the above one-pass and multi-pass imaging algorithms, there are mainly two kinds of methods to obtain 3D information from 2D images. The first kind of method, presented by Oriot and Hubert [16], is to divide the full aperture single-pass data into several subapertures, and find pixel displacements between different sub-aperture 2D images to calculate the height of target. However, the matching operation used in finding pixel displacements is not only time-consuming due to pixel-by-pixel operation but also difficult due to the different projected shape and amplitude on different sub-aperture 2D images. In addition, for real anisotropic targets, this limited azimuthal persistence leads to a limited 3D resolution. The second kind method is the interferometric method presented by Ertin et al. [17, 18]. Multi-pass CSAR data are also divided into several subapertures and the phase of 2D image sequence for the same subaperture is processed by the extended version of interferometry to get the height information with parametric spectral estimation used. With the relationship between height information and the corresponding 2D image coordinates, 3D target coordinates can be obtained. But the pre-condition is that the difference between the elevation angles for the different passes is small enough so that for each elevation pass target falls into the same resolution cell, and the elevation spacing should be uniform.

In this paper, we propose a 3D imaging algorithm with two-pass CSAR data. Firstly, both of the two full-aperture CSAR data are divided into several subapertures in the same way. Secondly, for each subaperture, the height of target is obtained by relating pixel displacements between two-pass 2D subimage pair on the same focal planes to those between two 2D subimages on different focal planes with the same single pass sub-aperture observation. Thirdly, based on the height information and 2D image coordinates, 3D target coordinates can be obtained for each subaperture. Finally, the reconstructed 3D subimages from all the subapertures are used to compose the final 3D reconstruction image just by combing them together. This algorithm makes use of two-pass information rather than single pass data to overcome the limited azimuthal persistence for real anisotropic targets, and needs not to assume that target falls into the same resolution cell for each elevation pass.

The rest of the paper is organized as follows. In Section 2, 2D imaging including 3D information for CSAR is discussed. A 3D target reconstruction algorithm with two-pass CSAR data is presented in Section 3. The imaging results about point target and backhoe data validating the new algorithm are shown in Section 4. Finally, Section 5 concludes the paper.

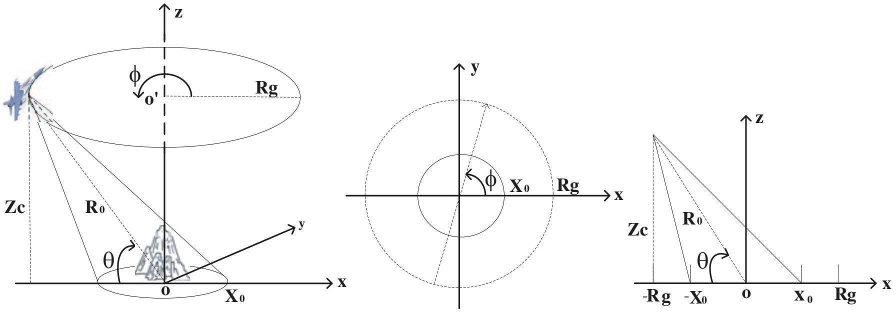

(a) (b) (c)

Figure 1. (a) Geometry of CSAR imaging system. (b) Top view. (c) Side view.

2. TWO-DIMENSIONAL IMAGING FOR CSAR

2.1. System Model

The CSAR imaging geometry is shown in Fig. 1(a). Its top view and side view are shown in Figs. 1(b) and (c), respectively. Let's denote the radar height as z_c and the flight radius as R_g. Then the slant range can be expressed as,

$$R_0 = \sqrt{R_g^2 + z_c^2} \tag{1}$$

and the slant depression angle can be calculated by

$$\theta = \arctan(\frac{z_c}{R_g}) \tag{2}$$

Let's further denote the transmitted radar signal as $p(t)$ and define the reflectivity function of target as $f(x, y, z)$ as shown in Fig. 1, where the height z is the function of (x, y), i.e., $z(x, y)$. Then the received echo signal can be given by [1],

$$\begin{aligned} s(t, \phi) = \int_y \int_x f(x, y, z(x, y)) \\ p\left[t - \frac{2\sqrt{(x-R_g\cos\phi)^2+(y-R_g\sin\phi)^2+(z(x,y)-z_c)^2}}{c}\right] dxdy \end{aligned} \tag{3}$$

The Fourier transform of (3) with respect to the fast-time t can be expressed as,

$$\begin{aligned} s(\omega, \phi) = P(\omega)\int_y\int_x f(x, y, z(x, y)) \\ \exp\left(-j2k\sqrt{(x-R_g\cos\phi)^2+(y-R_g\sin\phi)^2+(z(x,y)-z_c)^2}\right) dxdy \end{aligned} \tag{4}$$

where ω denotes the fast-time frequency, ϕ denotes the azimuthal angle, $P(\omega)$ denotes the Fourier transform of $p(t)$, $k = \frac{\omega}{c}$ and $c = 3 \times 10^8\,\mathrm{m/s}$.

2.2. 2D Imaging of One Point Target

In this section, we shall discuss about the relationship between 3D target coordinates and 2D image coordinates of an isotropic point target.

The geometry is shown in Fig. 2. Assume conditions of a wide bandwidth radar and far-field are satisfied. When the focal plane z_f is chosen as the height z of the target $P(x, y, z)$, i.e., $z_f = z$, the 2D image about the target is a focused point; otherwise, when $z_f \neq z$, the result shall be a defocused ring. This conclusion can be illustrated by the following simulation experiment. In the simulation, the target is located at (0, 0.1 m, 0), and the used parameters are listed in Table 1. Fig. 3(a) shows the 3D imaging result. Figs. 3(b)–(d) respectively show the 2D imaging results at different focal planes. It is obvious that when $z_f = 0$, the 2D imaging result of point target is a focused point and when $z_f \neq 0$, the result is a defocused ring.

Table 1. The system parameters.

Carrier frequency	10 GHz
Bandwidth	6 GHz
Radius of the flight track	200 m
Height of the radar	200 m
Radius of imaging area	0.2 m

In fact, there exists a relationship between the radius of defocused ring and the height of point target, which can be expressed by [22],

$$R \approx z \tan\theta \tag{5}$$

Based on Equation (5), another relationship between 3D point target coordinates (x, y, z) and its 2D image coordinates (x_l, y_l) can be written as,

$$\begin{cases} x_l = x + z \cdot \tan\theta \cos\phi \\ y_l = y + z \cdot \tan\theta \sin\phi \end{cases} \tag{6}$$

2.3. The Transformation between 2D Images on Different Focal Planes

In Section 2.2, different imaging results are obtained when different focal planes are chosen. However, the information included in these

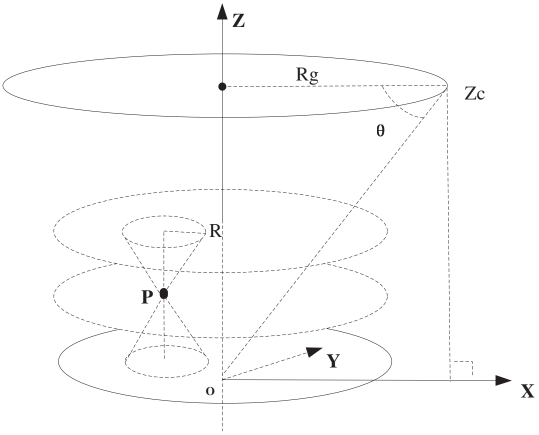

Figure 2. 2D imaging of one point target including 3D information.

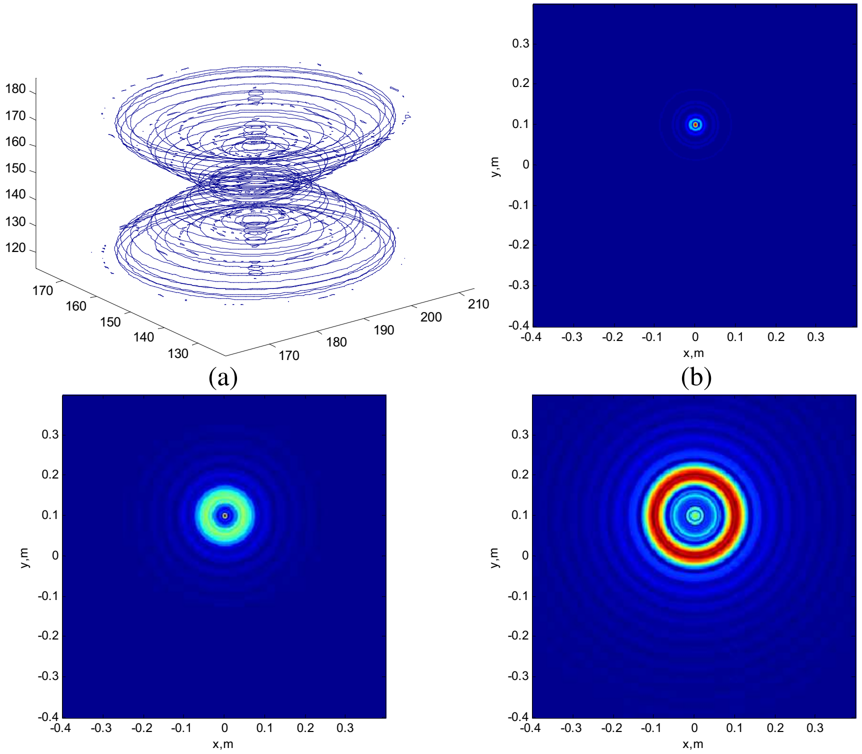

(a) (b)

(c) (d)

Figure 3. (a) 3D imaging result. 2D image on the focal plane, (b) $Z_f = 0\,\mathrm{m}$, (c) $Z_f = 0.025\,\mathrm{m}$, (d) $Z_f = 0.05\,\mathrm{m}$.

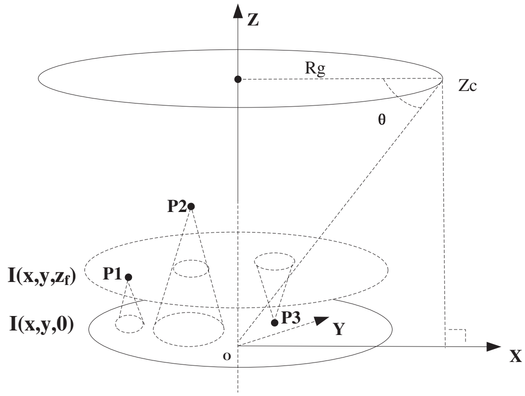

Figure 4. The transformation between 2D images on different focal planes.

images is same since the flight pass is unchanged, and any one of them $I(x_l, y_l, z_f)$ can be regenerated from the image $I(x_l, y_l, 0)$ on the focal plane $z_f = 0$ when the condition $|z_f| \ll R_0$ is satisfied. The transformation process is as follows [1, 17],

$$I(x_l, y_l, z_f) = \mathbb{F}_{x,y}^{-1}\left[\mathbb{F}_{x,y}\left[I(x_l, y_l, 0)\right]\exp\left(-j\sqrt{k_x^2 + k_y^2}\tan\theta z_f\right)\right] \quad (7)$$

where $\left\{\begin{array}{l} k_x = \frac{\omega}{c}\cos\theta\cos\phi \\ k_y = \frac{\omega}{c}\cos\theta\sin\phi \end{array}\right.$.

The geometry of 2D image $I(x_l, y_l, z_f)$ regenerated from image $I(x_l, y_l, 0)$ is shown in Fig. 4. The height locations of three isotropic point targets $P1$, $P2$ and $P3$ are $z = z_f$, $z \neq z_f$,0, and $z = 0$, respectively. When $I(x_l, y_l, z_f)$ is regenerated from $I(x_l, y_l, 0)$, $P1$ is transformed from a defocused ring to a focused point, $P3$ is transformed from a focused point to a defocused ring, and $P2$ is transformed from a defocused ring to another defocused ring with a different radius. This transformation process can also be proved by the following simulation experiment. The parameters are listed in Table 2, and three targets are respectively located at (−1 m, 1 m, 0.2 m), (0, 0.05 m, 1 m), and (1.2 m, 0, 0). Figs. 5(a) and (c) show 2D images on the focal planes $z_f = 0$ and $z_f = 0.2\,\text{m}$, respectively. Fig. 5(b) is regenerated from Fig. 5(a). It is obvious that Figs. 5(b) and (c) are almost the same.

Table 2. The system parameters.

Carrier frequency	10 GHz
Bandwidth	6 GHz
Radius of the flight track	200 m
Height locations of the radar	200 m, 240 m
Radius of imaging area	0.2 m

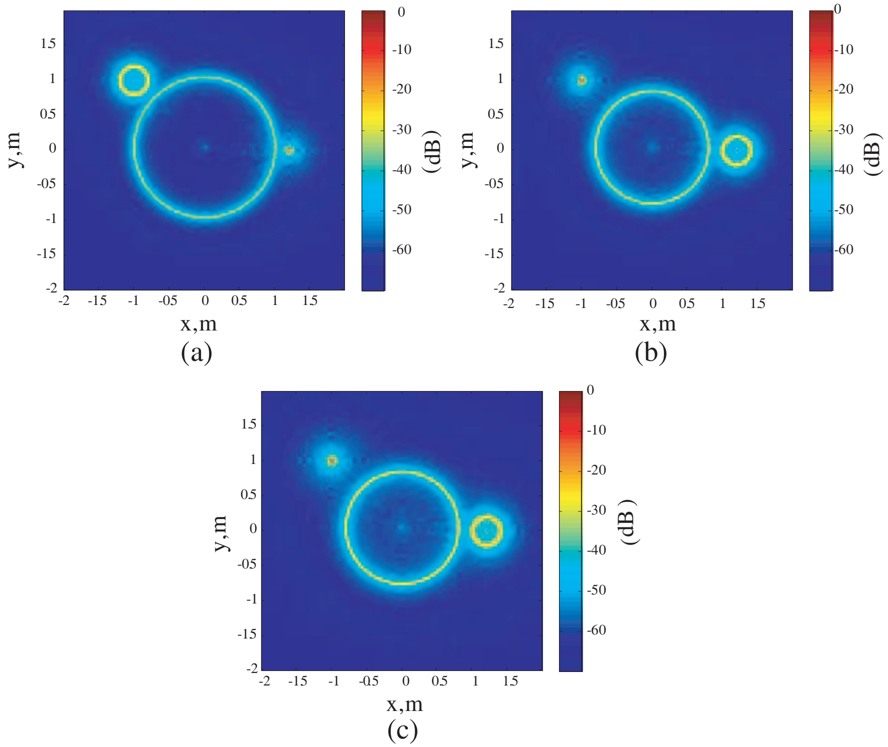

(a) (b) (c)

Figure 5. (a) 2D image on the focal plane $Z_f = 0$. (b) The focal plane is transformed from $Z_f = 0$ to $Z_f = 0.2\,\mathrm{m}$. (c) 2D image on the focal plane $Z_f = 0.2\,\mathrm{m}$.

3. A 3D TARGET RECONSTRUCTION ALGORITHM BASED ON TWO-PASS CSAR OBSERVATIONS

3.1. The Principle

In Section 2.2, if the depression angle θ changes, then 2D image coordinates (x_l, y_l) in Equation (6) will also change. Therefore, there should be pixel displacements between the 2D images of two passes on the same focal planes. In Section 2.3, although only single pass CSAR data is used, there are pixel displacements between two 2D images on different focal planes. In this section, we will establish the relationship between pixel displacements in these two cases.

Case A: The geometry is shown in Fig. 6. The ground plane is chosen as the focal plane, i.e., $z_f = 0$.

For the first pass, the height of radar is Zc_1 and the depression angle is $\theta_1 = \arctan(Zc_1/Rg)$. The location relationship between 3D target $P(x, y, z)$ and its 2D image $P_1(x_{l1}, y_{l1})$ can be written as,

$$\left\{\begin{array}{l} x_{l1} = x + z \cdot \tan\theta_1 \cos\phi \\ y_{l1} = y + z \cdot \tan\theta_1 \sin\phi \end{array}\right. \tag{8}$$

For the second pass, the height of radar is Zc_2 and the depression angle is $\theta_2 = \arctan(Zc_2/Rg)$. The location relationship between 3D target $P(x, y, z)$ and its 2D image $P_2(x_{l2}, y_{l2})$ can be written as,

$$\left\{\begin{array}{l} x_{l2} = x + z \cdot \tan\theta_2 \cos\phi \\ y_{l2} = y + z \cdot \tan\theta_2 \sin\phi \end{array}\right. \tag{9}$$

By subtracting Equation (8) from Equation (9), the pixel displacements between P_1 and P_2 can be obtained as,

$$\left\{\begin{array}{l} \Delta x_l = x_{l2} - x_{l1} = z\cos\phi(\tan\theta_2 - \tan\theta_1) \\ \Delta y_l = y_{l2} - y_{l1} = z\sin\phi(\tan\theta_2 - \tan\theta_1) \end{array}\right. \tag{10}$$

Case B: The geometry is shown in Fig. 7. Only the second pass data is used in imaging.

When the focal plane is $z_f = 0$, the result is the same as Equation (9) indicated. When the focal plane is $z_f = h$, the location relationship between 3D target $P(x, y, z)$ and its 2D image $P_2'(x_{l2\_new}, y_{l2\_new})$ can be written as,

$$\left\{\begin{array}{l} x_{l2\_new} = x + (z - h) \cdot \tan\theta_2 \cos\phi \\ y_{l2\_new} = y + (z - h) \cdot \tan\theta_2 \sin\phi \end{array}\right. \tag{11}$$

By subtracting Equation (11) from Equation (9), the pixel displacements between P_2 and P_2' can be obtained as,

$$\left\{\begin{array}{l} \Delta x_{l\_new} = x_{l2} - x_{l2\_new} = h\tan\theta_2\cos\phi \\ \Delta y_{l\_new} = y_{l2} - y_{l2\_new} = h\tan\theta_2\sin\phi \end{array}\right. \tag{12}$$

If the pixel displacements in case A and case B are equal to each other,

$$\left\{\begin{array}{l} \Delta x_{l\_new} = \Delta x_l = h\tan\theta_2\cos\phi = z\cos\phi(\tan\theta_2 - \tan\theta_1) \\ \Delta y_{l\_new} = \Delta y_l = h\tan\theta_2\sin\phi = z\sin\phi(\tan\theta_2 - \tan\theta_1) \end{array}\right. \tag{13}$$

then the height of target can be calculated by the following equation,

$$z = h\tan\theta_2/(\tan\theta_2 - \tan\theta_1) \tag{14}$$

3.2. Description of Algorithm

From Equation (14), the depression angles of θ_1 and θ_2 can be calculated according to system parameters, so the key to reconstruct the height of target is to obtain the focal plane parameter h. The algorithm is based on CLEAN technique [23, 24], which removes the strongest scatterer on the 2D images each time, and the detailed description of the algorithm steps are as follows,

(1) Divide the full aperture data into subapertures and each one is with a few degree of azimuthal angle range.

(2) Choose the focal plane $z_f = 0$, and reconstruct 2D images of I_1 and I_2 for each subaperture, which corresponds to two-pass CSAR observations, respectively.

(3) Set the height range to be $[-H, H]$, and the height spacing to be ΔH. Then calculate the total number of transformation $N = \frac{2H}{\Delta H}$, and regenerate 2D image sequence $I'_{2(i)}$, $i = 1, 2, \ldots, N$ from I_2 at different focal height.

(4) Set the iterative parameters as $k = 1$, $I_{1k} = I_1$, $I_{2k} = I_2$, $I'_{2k(i)} = I'_{2(i)}$, $i = 1, 2, \ldots, N$, as well as the total number of iterations M and the residual energy threshold ratio Thr_Ratio, and then calculate the residual energy threshold Thr through $Thr = Thr\_Ratio \times \sum\left(|I_1|^2\right)$.

(5) Search the maximum amplitude $A_{k\_\max}$ of I_{1k} and their image coordinates (x_pos, y_pos), and then normalize I_{1k} with respect to $A_{k\_\max}$.

(6) Normalize $I'_{2k(i)}$ and get the amplitude of $I'_{2k(i)}$ at (x_pos, y_pos).

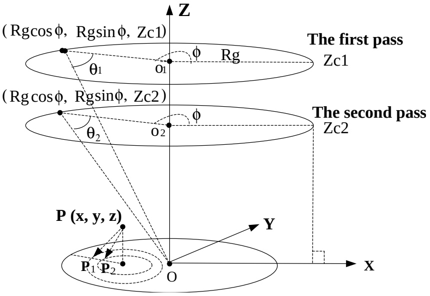

Figure 6. 2D imaging results of two-pass CSAR observations on the same focal plane.

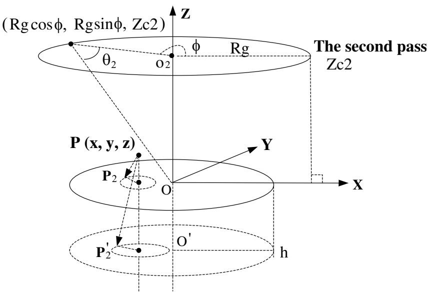

Figure 7. 2D imaging results of the second pass CSAR observation on different focal planes.

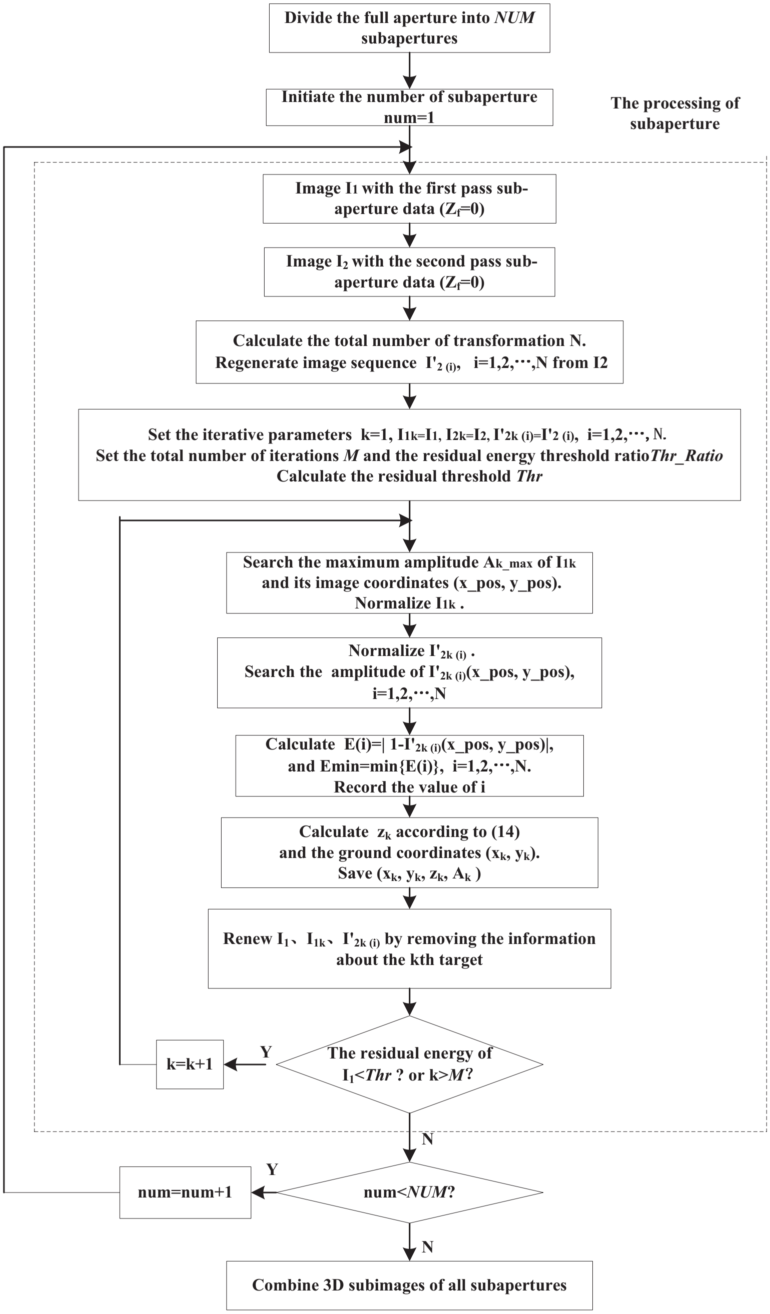

Figure 8. Flow diagram of the presented algorithm.

Table 3. The system parameters.

Carrier frequency	10 GHz
Bandwidth	6 GHz
Radius of the flight track	200 m
Height locations of the radar	200 m, 240 m
Radius of imaging area	2 m

Table 4. Original point targets.

Scatter No.	$(x,\ y,\ z)$ (m)	Amplitude
1	(0, 0, 0)	1
2	(0, 0.75, 0.1)	1
3	(0.75, 0, 0.1)	1
4	(0, 0, 0.3)	1
5	(0, 0, −0.3)	1

(7) Calculate the difference between the maximum of I_{1k} and $I'_{2k(i)}(x\_pos, y\_pos)$, i.e., $E(i) = \left|1 - I'_{2k(i)}(x\_pos, y\_pos)\right|$. Then calculate $E_{\min} = \text{Min}\left\{E(i)\right\}$ and record the value of i.

(8) Calculate the height of focal plane through $h_k = -H + i \times \Delta H$, and then calculate the height of target through $z_k = h_k \tan\theta_2/(\tan\theta_2 - \tan\theta_1)$ according to Equation (14). Further calculate the target coordinates (x_k, y_k) through $\left\{ \begin{array}{l} x_k = x\_pos - z_k \cdot \tan\theta_1 \cos\phi \\ y_k = y\_pos - z_k \cdot \tan\theta_1 \sin\phi \end{array} \right.$. Save the locations and amplitude of the kth target (x_k, y_k, z_k, A_k).

(9) Renew I_1, I_{1k} and $I'_{2k(i)}$ by removing the information about the kth target.

(10) If the residual energy of I_1 i.e., $\sum\left(|I_1|^2\right)$ is smaller than Thr, or the iterative number is larger than M, then update the iterative number and proceed to the next subaperture; otherwise, repeat steps (5)–(9).

(11) Repeat steps (2)–(10) until all subapertures are processed.

(12) Combine 3D subimages of all subapertures to get the final 3D image.

The flow diagram of the algorithm is shown in Fig. 8, and the processing steps in dashed rectangular are for subaperture imaging.

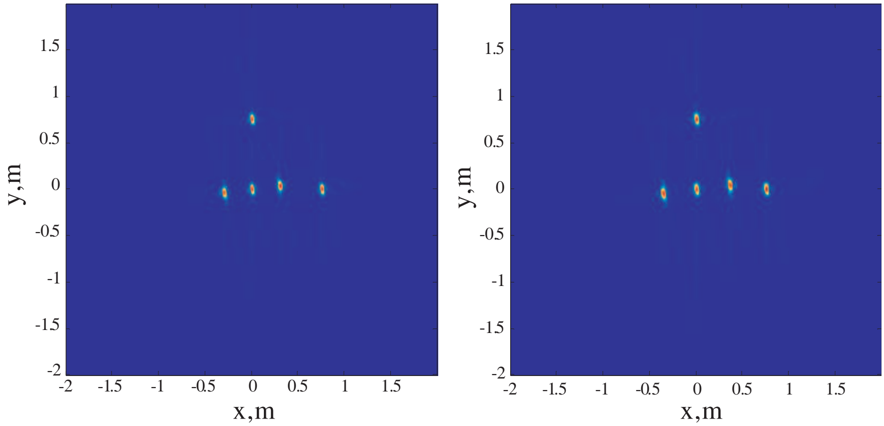

(a) (b)

Figure 9. 2D image with (a) the first pass sub-aperture data (b) the second pass sub-aperture data.

Table 5. Reconstructed point targets and the corresponding errors for the first subaperture.

Scatter No.	(x, y, z) (m)	Amplitude	(Δx, Δy, Δz) (m)	ΔAmplitude
1	(0.0107, 0.0107, 0)	1	(0.0107, 0.0107, 0)	0
2	(0.0107, 0.7614, 0)	0.9767	(0.0107, 0.0114, 0)	− 0.0233
3	(0.7614, 0.0107, 0)	0.9628	(0.0114, 0.0107, 0)	−0.0372
4	(0.0087, 0.0101, 0.3047)	0.9587	(0.0087, 0.0101, 0.0047)	− 0.0413
5	(−0.0105, 0.0084, −0.2813)	0.9528	(− 0.0105, 0.0084, 0.0187)	− 0.0472

4. SIMULATION RESULTS

4.1. Point Targets

The simulation parameters are listed in Table 3, and original target coordinates are list in Table 4. Both of two-pass full 360° aperture echo data of five targets are divided into 25 subapertures. Figs. 9(a) and (b) present the imaging results of the first subapertures of two-pass observations, respectively, Figs. 10(a)–(d) present the constructed 3D image and its projections onto different planes. In the same manner, one can get all other 3D images and their projections. Figs. 11(a)–(d) present the final images after combining all subaperture images together. For the first subaperture, the reconstructed point targets and the corresponding errors are listed in Table 5.

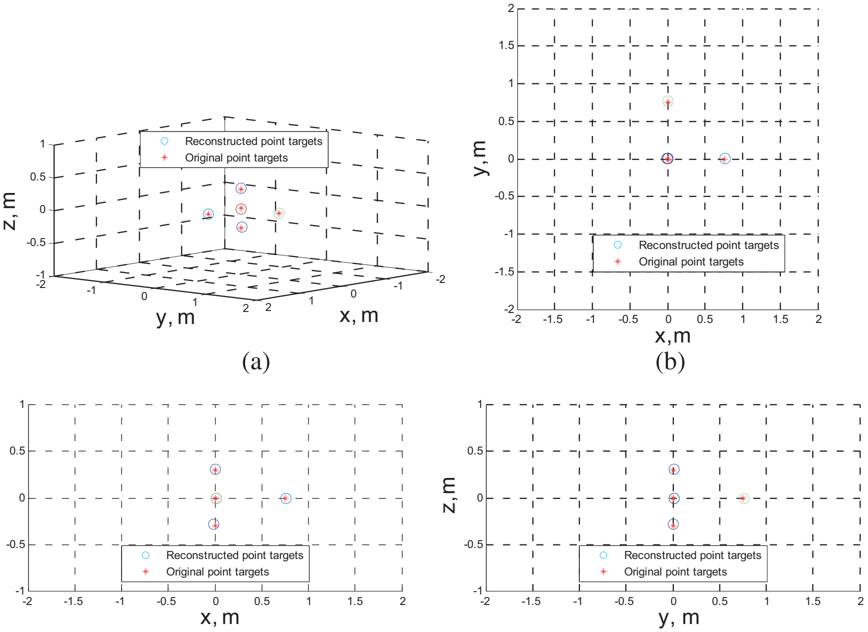

(a) (b)

(c) (d)

Figure 10. (a) 3D reconstructed image of the first subaperture. Projected image on (b) X-Y plane, (c) X-Z plane, (d) Y-Z plane.

From Fig. 10 one can see that all the targets are almost reconstructed correctly. In Table 5, both reconstructed target coordinates (x, y, z) and amplitudes are compared with the original. Their errors are denoted as (Δx, Δy, Δz) and ΔAmplitude respectively. Errors about target coordinates may come from (1) the approximate radius R of defocused ring in Equation (5); (2) the approximate azimuthal angle ϕ for each subaperture; (3) the quantization error of height H. Errors about amplitudes are mainly from the different energy distribute of targets with different height in the same 2D image.

In Fig. 11, some targets are seemed to be reconstructed many times while others are seemed to be reconstructed only one time. In fact, all targets are reconstructed 25 times, each by one subaperture. If the reconstructions from some different subapertures are the same, they will overlap with each other in the composite image, and if they are different, then there is no overlap in the composite image. When apply this 3D reconstruction algorithm to real anisotropic targets, they may be reconstructed only few times because of the limited azimuthal persistence over the full aperture.

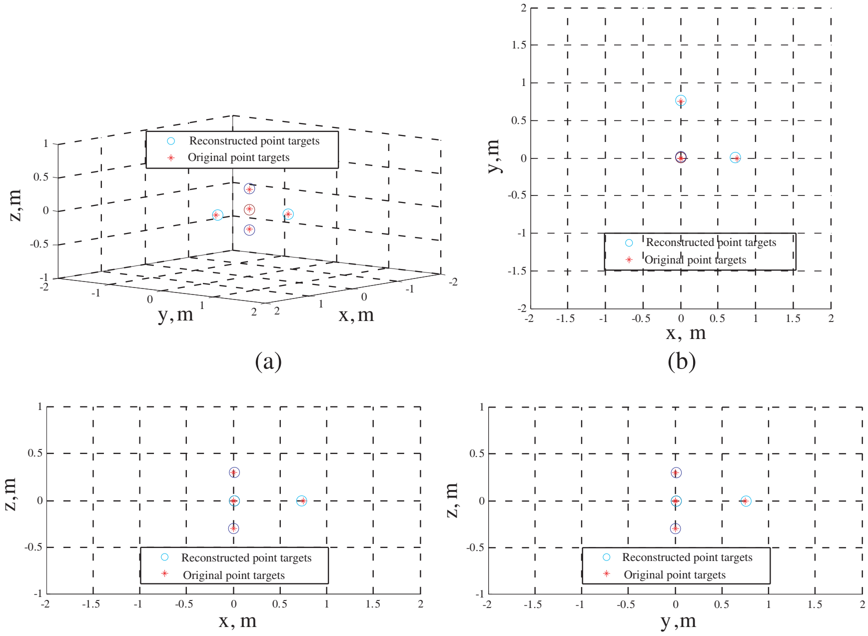

(a) (b)

(c) (d)

Figure 11. (a) 3D reconstructed image of the full aperture. Projected image on (b) X-Y plane, (c) X-Z plane, (d) Y-Z plane.

4.2. Backhoe Data

Backhoe data is generated using XpatchF electromagnetic scattering prediction software [19]. It have been generated for 8–12 GHz frequency range, 0°–360° azimuth range, and 0°–90° incident angle range. Fig. 12 shows the 3D CAD model and its projection on different planes. Only parts of two-pass data were published on the website [25]. Two depression angles are 0° and 30°, respectively, and both of them have angles 100°–250° in azimuth. 2D composite images of the two data sets are shown in Figs. 13(a) and (b) respectively. Comparing these two images, one can see that the image at 30° depressing angle is much blurred than that at 0° depressing angle as well as the scattering strength is much stronger. In order to achieve 3D reconstruction, both of the two-pass part aperture echo data are first divided into 29 subapertures. Then 2D image pairs corresponding to same subapertures are utilized to reconstruct 3D subimages. At last, the final 3D image is formed by combing all of the 3D subimages. The 3D image and its projected 2D images are respectively shown in Figs. 14(a)–(d). The 3D reconstructed image of Fig. 14(a) is shown in

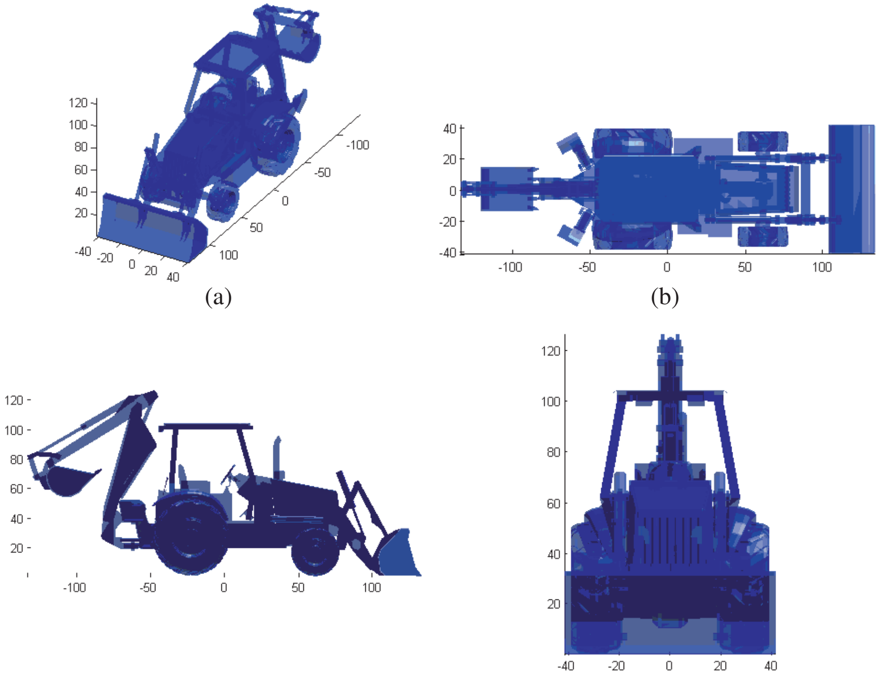

(a) (b)

(c) (d)

Figure 12. (a) 3D backhoe model. Projected model on (b) *X*-*Y* plane, (c) *X*-*Z* plane, (d) *Y*-*Z* plane.

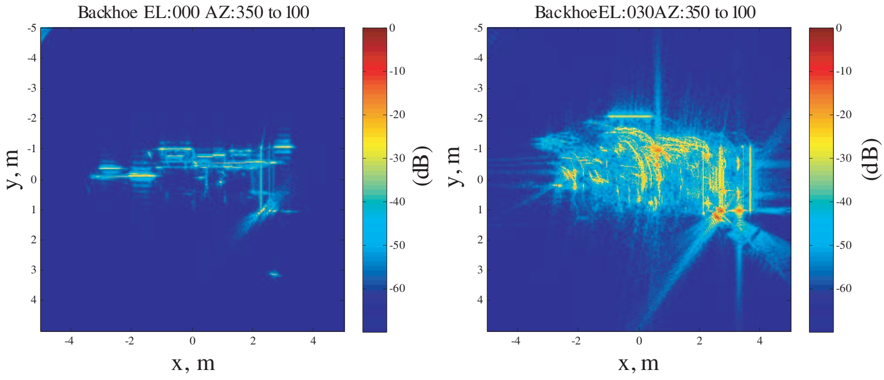

(a) (b)

Figure 13. 2D composite image with (a) depression angle 0°, (b) depression angle 30°.

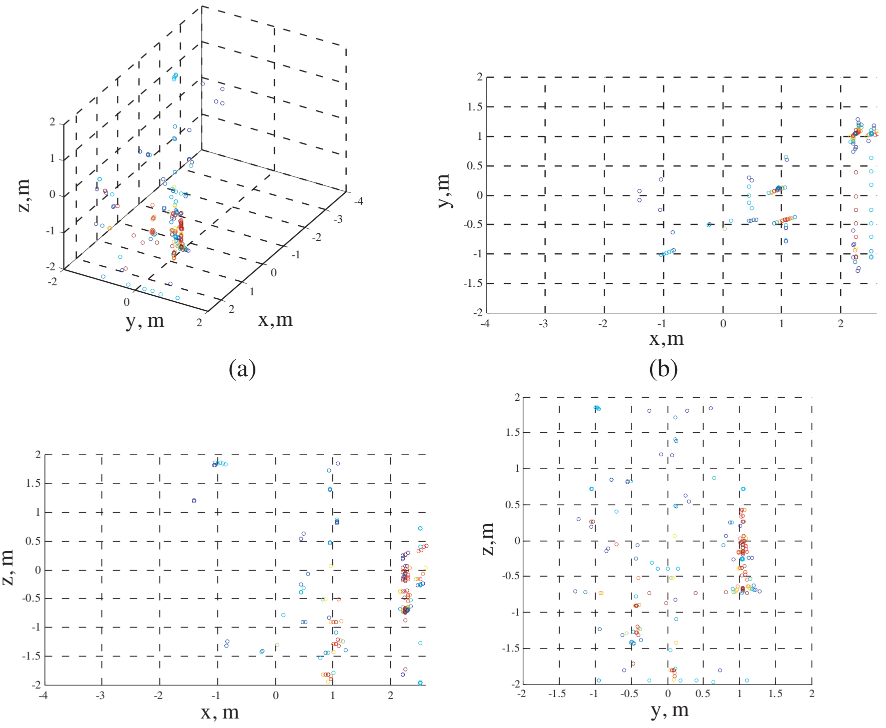

(a)

(b)

(c)

(d)

Figure 14. (a) 3D reconstructed image. Projected image on (b) X-Y plane, (c) X-Z plane, (d) Y-Z plane.

the same viewing angle as Fig. 12(a) shown, and Figs. 14(b), (c), and (d) are shown in same viewing angles as Figs. 12(b), (c), and (d) shown. By comparing these image pairs, one can see that the reconstructed 3D image partially reflects the real 3D structure of the target, i.e., some parts of the target structure are reconstructed well, but some parts are not or even missed. The main reason is the depressing angles of two passes are much different and results in much less common points between subimage pairs. Totally speaking, as one can see that the outline of the backhoe has been reconstructed.

5. CONCLUSION

In this paper, a new algorithm performing 3D target reconstruction based on two-pass CSAR data is presented. Different from other 3D imaging algorithms from 2D images, the proposed algorithm makes use of two-pass data rather than single pass data to overcome the limited azimuthal persistence for real anisotropic targets, and does not need to assume target falls into the same resolution cell for each elevation pass. For each subaperture, the height of target is reconstructed through the relationship between the pixel displacements in the image pair of two observations and the pixel displacements in the image pair of one observation on two different focal planes, and then 3D target coordinates can be obtained based on the retrieved height information and the 2D image coordinates. Both imaging results about point targets and backhoe data show effectiveness of the presented algorithm.

We should point out that, as other 3D targets reconstruction algorithms from 2D images do, the algorithm will fail when overlay occur on 2D images. If locations of the maximum amplitudes of different targets in the overlaid area occur in the same resolution cell on 2D image, then only the location of one target can be reconstructed; otherwise, both amplitudes and locations of these targets can not be reconstructed correctly. We shall do further work to deal with these cases.

REFERENCES

1. Soumekh, M., *Synthetic Aperture Radar Signal Processing with MATLAB Algorithms*, Wiley, New York, 1999.
2. Ishimaru, A., T. K. Chan, and Y. Kuga, "An imaging technique using confocal circular synthetic aperture radar," *IEEE Transactions on Geoscience and Remote Sensing*, Vol. 36, No. 5, 1524–1530, Sep. 1998.
3. Cantalloube, H. M. J., E. Colin-Koeniguer, and H. Oriot. "High resolution SAR imaging along circular trajectories," *IEEE International Geoscience and Remote Sensing Symposium*, 2007.
4. Cantalloube, H. M. J., H. Oriot, and E. ColinKoeniger, "Physic and experimental issues on high resolution SAR imaging of urban area," *IEEE International Geoscience and Remote Sensing Symposium*, 2008.
5. Frölind, P.-O. U. and M. H. Lars, *First Results on VHF-band SAR Imaging using Circular Tracks*, EUSAR, Gustavsson, Anders (Swedish Defence Research Agency), 2008.
6. Hantscher, S., et al., "94 GHz person scanner with circular aperture as part of a new sensor concept on airports," *11th International Radar Symposium*, 2010.
7. Tan, W. X., W. Hong, Y. P. Wang, and Y. R. Wu, "A novel spherical-wave three-dimensional imaging algorithm

for microwave cylindrical scanning geometries," *Progress In Electromagnetics Research*, Vol. 111, 43–70, 2011.

8. Liu, Q., W. Hong, W. X. Tan, Y. Lin, Y. P. Wang, and Y. R. Wu, "An improved polar format algorithm with performance analysis for geosynchronous circular SAR 2D imaging," *Progress In Electromagnetics Research*, Vol. 119, 155–170, 2011.
9. Chan, Y. K. and V. C. Koo, "An introduction to synthetic aperture radar (SAR)," *Progress In Electromagnetics Research B*, Vol. 2, 27–60, 2008.
10. Moreira, A., J. Mittermayer, and R. Scheiber, "Extended chirp scaling algorithm for air- and spaceborne SAR data processing in stripmap and ScanSAR imaging modes," *IEEE Transactions on Geoscience and Remote Sensing*, Vol. 34, No. 5, 1123–1136, Sep. 1996.
11. Fortuny, J. and J. M. Lopez-Sanchez, "Extension of the 3-D range migration algorithm to cylindrical and spherical scanning geometries," *IEEE Transactions on Antennas and Propagation*, Vol. 49, No. 10, 1434–1444, 2001.
12. Guo, D. M., H. P. Xu, and J. W. Li, "Extended wavenumber domain algorithm for highly squinted sliding spotlight SAR data processing," *Progress In Electromagnetics Research*, Vol. 114, 17–32, 2011.
13. Soumekh, M., "Reconnaissance with slant plane circular SAR imaging," *IEEE Transactions on Image Processing*, Vol. 5, No. 8, 1252–1265, 1996.
14. Cantalloube, H. M. J., P. Dubois-Fernandez, and X. Dupuis. "Very high resolution SAR images over dense urban area," *IEEE International Geoscience and Remote Sensing Symposium*, 2005.
15. Pinheiro, M., et al., "Tomographic 3D reconstruction from airborne circular SAR," *IEEE International Geoscience and Remote Sensing Symposium*, 2009.
16. Oriot, H. and C. Hubert, "Circular SAR imagery for urban remote sensing," *EUSAR*, 2008.
17. Ertin, E., et al., "GOTCHA experience report: Three-dimensional SAR imaging with complete circular apertures," *Proc. SPIE Algorithms for Synthetic Aperture Radar Imagery XIV*, Vol. 6568, 656802, 2007.
18. Ertin, E., R. L. Moses, and L. C. Potter, "Interferometric methods for three-dimensional target reconstruction with multipass circular SAR," *Radar, Sonar & Navigation*, IET, Vol. 4, No. 3, 464–473, 2010.

19. Ertin, E., L. C. Potter, and R. L. Moses, "Enhanced imaging over complete circular apertures," *Fortieth Asilomar Conference on Signals, Systems and Computers*, 2006.
20. Austin, C. D., E. Ertin, and R. L. Moses, "Sparse multipass 3D SAR imaging: Applications to the GOTCHA data set," *Proc. SPIE Algorithms for Synthetic Aperture Radar Imagery XVI*, Vol. 7337, 733703, 2009.
21. Potter, L. C., et al., "Sparsity and compressed sensing in radar imaging," *Proceedings of the IEEE*, Vol. 98, No. 6, 1006–1020, 2010.
22. Moore, L. J. and L. C. Potter, "Three-dimensional resolution for circular synthetic aperture radar," *Proc. SPIE Algorithms for Synthetic Aperture Radar Imagery XIV*, Vol. 6568, 656804, 2007.
23. Ranjan, B., "Two-dimensional evolutionary programming-based CLEAN," *IEEE Transations on Aerospace and Electronic Systems*, Vol. 39, No. 1, 373–382, 2003.
24. Camps, A., J. Bar'a, F. Torres, and I. Corbella, "Extension of the clean technique to the microwave imaging of continuous thermal sources by means of aperture synthesis radiometers," *Progress In Electromagnetics Research*, Vol. 18, 67–83, 1998.
25. http://eaton.math.rpi.edu/CourseMaterials/Cheney/backhoe/.